What does the impurity variability at the microscale represent in ice cores? Insights from a conceptual approach

Piers Larkman[1], Rachael H. Rhodes[2], Nicolas Stoll[1], Carlo Barbante[1,3], and Pascal Bohleber[1,4]

[1]Department of Environmental Sciences, Informatics and Statistics, Ca'Foscari University of Venice, Venice, Italy
[2]Department of Earth Sciences, University of Cambridge, Cambridge, United Kingdom
[3]Institute of Polar Sciences, National Research Council (CNR-ISP), Venice Mestre, Italy
[4]Department of Geosciences, Alfred Wegener Institute Helmholtz Centre for Polar and Marine Research, Bremerhaven, Germany

Correspondence: Piers Larkman (piersmichael.larkman@unive.it)

Abstract. Measuring aerosol-related impurities in ice cores gives insight into Earth's past climate conditions. In order to resolve highly thinned layers and to investigate post-depositional processes, such measurements require high-resolution analysis, especially in deep ice. Micron-resolution impurity data can be collected using laser ablation inductively coupled plasma mass spectrometry (LA-ICP-MS) but this requires careful assessment to avoid misinterpretation. 2D imaging with LA-ICP-MS
5   has provided significant new insight, often showing an association between soluble impurities and the ice crystal matrix, but interpreting 1D signals collected with LA-ICP-MS remains challenging partially due to this impurity-boundary association appearing in the high-frequency component of signals. In this work, a computational framework has been developed integrating insights from 2D imaging to aid the interpretation of 1D signals. The framework utilises a simulated model of a macroscopic ice volume with a representative microstructure and soluble impurity localisation that statistically represents distributions seen
10 in 2D maps, allowing quantitative assessment of the imprint of the ice matrix on 1D signals collected from the volume. Input data were collected from four ice core samples from Greenland and Antarctica. For the samples measured, quantifying the variability of 1D signals due to the impurity-matrix imprint shows that modelled continuous bulk signal intensity at the centimetre scale varies below 2 % away from an idealised measurement that captures all variability. In contrast, modelled single-profile micron-resolution LA-ICP-MS signals can vary by more than an average of 100 %. Combining individual LA-ICP-MS signals
15 into smoothed and spatially averaged signals can reduce this variation to between 1.5 and 5.9 %. This approach guides collecting layer-representative signals from LA-ICP-MS line profiles and may help to bridge the scale gap between LA-ICP-MS data and data collected from meltwater analysis.

1 Introduction

Ice cores collected from Earth's polar regions contain invaluable information relating to its climate system, with continuous
20 records reaching back as far as 800,000 years (Loulergue et al., 2008; Brook and Buizert, 2018). Analysis of well-preserved
old ice, such as that targeted in the Beyond EPICA drilling on the Antarctic Plateau, aims to extend this record back to
approximately 1.5 million years (Chung et al., 2023). Ice sections originating from near the bottom of ice sheets, including
that targeted for the Beyond EPICA core, contain very thinned layers, with many thousands of years of climate information
compressed into small vertical sections. Such ice will have undergone significant post-depositional changes.

25 A subject of interest within these cores are the aerosol-related impurities in the ice (e.g. Legrand and Mayewski, 1997), which
can be used as a proxy to reconstruct past climate conditions over timescales ranging from seasonal to millennial. A widely
employed technique for collecting such signals is continuous flow analysis (CFA), which outputs a one-dimensional (1D)
impurity signal along the down-core axis at centimetre depth resolution (Kaufmann et al., 2008). An example target impurity
is sodium, for which potential links to sea ice extent are discussed (Abram et al., 2013). As there are likely more than 14 ka of
30 ice per metre in the deep ice of the Beyond EPICA core, high-resolution analysis is key to deciphering climate signals in these
highly thinned sections. Such analysis will require resolutions beyond that delivered by CFA while also carefully assessing the
impact of post-depositional changes of impurity localisation.

To measure impurity signals at micron-resolution, laser ablation inductively coupled plasma mass spectrometry (LA-ICP-MS)
was applied to ice core analysis (Reinhardt et al., 2001). Ablating ice in its solid form, LA-ICP-MS preserves information
35 on impurity location in the ice matrix while analysing the surface of the sample (Müller et al., 2011). Two-dimensional (2D)
state-of-the-art imaging of impurities using LA-ICP-MS has shown that the location of (mostly soluble) impurities, such as
sodium and magnesium, can significantly correlate with the location of boundaries between crystals in the ice matrix (Stoll
et al., 2023; Bohleber et al., 2020). This impurity-boundary association imprints onto 1D line profile signals collected along the
down-core axis of samples, changing the resultant signal depending on the lateral position on the ice the signal is collected from
40 (Bohleber et al., 2021). It is now clear that this imprint obscures the interpretation of such profiles in the context of extracting a
climate signal, but the extent to which this occurs will depend on the degree of impurity localisation as well as grain size. The
micron-resolution and 2D data sampled from the surface with LA-ICP-MS greatly differs from the centimetre-resolution 1D
bulk impurity data obtained with CFA. Despite methodological differences in LA-ICP-MS and CFA, a phenomenological link
was made between 1D down-core signals collected using LA-ICP-MS and CFA (Della Lunga et al., 2017; Spaulding et al.,
45 2017), after applying heavy smoothing to LA-ICP-MS signals. Any explanation of this link between the two techniques must
come from an improved understanding of the chemical signals in ice across different length scales.

To allow exploration of how impurity localisation impacts signals, a computational framework that allows extensive analysis
of LA-ICP-MS and CFA data has been developed. This open-source framework[1] developed in python is designed to guide
experimental data collection, especially when attempting to capture layer signals with 1D LA-ICP-MS profiles. Generating

---

[1]Code available at https://github.com/Piers-Larkman/Ice_Impurities

a computational model of a macroscopic ice volume, comparable to the dimensions of a sample melted during CFA, that is statistically representative of grain and impurity properties revealed by 2D LA-ICP-MS imaging allows us to contrast modelled and empirical LA-ICP-MS data. This delivers insight on how the spatial distribution of soluble impurities impacts signal collection. Presenting this new conceptual approach, this paper aims to:

- Present 1D profiles and 2D intensity maps collected using LA-ICP-MS from sections of Antarctic and Greenland ice cores. Focusing on the mostly soluble impurities, we take sodium as an archetypal species in this context.

- Outline the theoretical foundation, computational implementation, and validation of a three-dimensional (3D) model that captures the localisation of soluble impurities in ice at the microscale, while being statistically representative at the macroscale.

- Establish an initial application of this model to investigate how the spatial distribution of soluble impurities impacts the representativeness of high-resolution centimetre length 1D signals taken along the down-core axis.

2 Methods

2.1 Overview

The general outline of the developed framework is visualised in Fig. 1. The computational representation uses the arguably most simple manifestation of a climate signal, a constant signal. All more complex signals can be constructed by adding small increments of such kind, which can be explored in future work. Optical and chemical data are collected with LA-ICP-MS, revealing the spatial distribution of soluble impurities, from here on referred to interchangeably with 'impurities', i.e. their localisation at the grain boundaries. The impurity distribution at grain boundaries and interiors is combined with mean grain size estimates parameterise the 3D model's generation of a macroscopic volume populated with impurities. 1D signals representing LA-ICP-MS or CFA measurements are simulated along the down-core axis of the modelled volume by recording, combining, and processing the intensity at each point in a vertical profile. Relying on the fact that the climate signal present in the modelled volume is an un-changing mean intensity, these signals are then analysed to understand how well they capture this underlying signal.

2.2 Sample selection

Samples were selected to cover a broad range of conditions, including both Greenland and Antarctica as well as glacial and interglacial periods. Four ice samples were analysed and modelled, two from the EPICA dome C (EDC) ice core (Stauffer et al., 2004) and two from the Renland Ice Cap Project (RECAP) ice core (Simonsen et al., 2019) (Table 1). Ages for EDC samples are from the AICC2023 timescale for the EDC ice core (Bouchet et al., 2023) and from the RECAP time scale for RECAP samples (Simonsen et al., 2019) and show samples originate from either the Holocene or Last Glacial Period (LGP). Grain radius data are taken from published values (EPICA community members, 2004) (Weikusat et al., 2024).
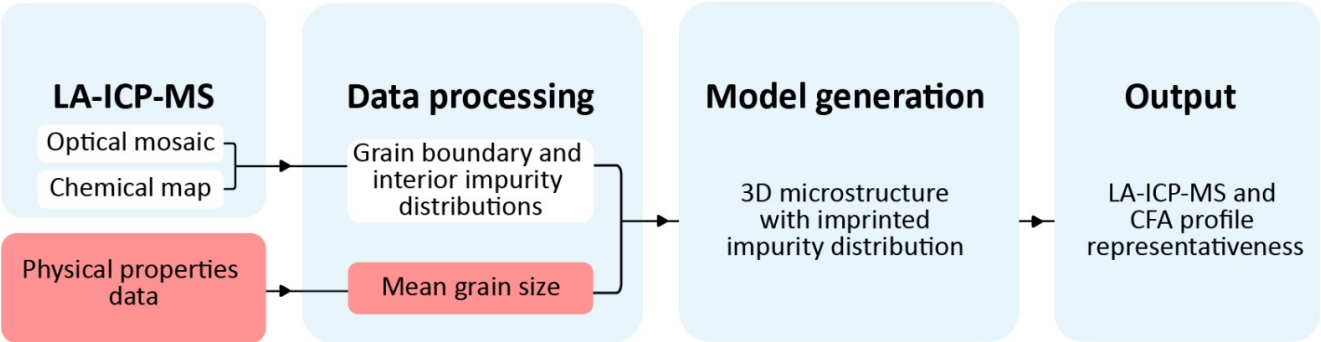
Figure 1. Flow chart detailing the framework operation. The mean grain size data for EDC and RECAP are from EPICA community members (2004) and Weikusat et al. (2024), respectively.

Table 1. Information on all analysed samples. Sample depth is the top of the sample, all relative depths discussed in the paper are reported with reference to this top depth. Grain radius is the mean effective spherical grain radius at the reported depth.

Ice core	EDC	EDC	RECAP	RECAP
Climate period	Holocene	LGP	Holocene	LGP
Top depth (m)	282.23	1096.45	495.18	536.70
Age (yr b1950)	9000	75000	5800	35000
Sample length (mm)	80	79	80	59
Mean grain radius (mm)	1.3	2.3	4.2	1.7
Number of LA-ICP-MS profiles measured	10	10	4	6
Profile lateral separation (mm)	80 to 6000	80 to 12000	1000 to 5000	1000 to 5000

yr b1950: years before 1950 CE

2.3 Experimental

2.3.1 Data collection

The LA-ICP-MS setup at the University of Venice was used adhering to current best practice for analysis on ice (Bohleber et al., 2024). The setup utilises an Analyte Excite ArF excimer 193 nm laser with a HelEx II two-volume ablation chamber (Teledyne CETAC Photon Machines) connected to an iCAP-RQ quadrupole ICP-MS (Thermo Scientific) using a rapid aerosol transfer line. Samples were prepared with a thickness of approximately $1\,cm$, a width of $2\,cm$ and lengths reported in Table 1. During analysis, samples were held at a stable temperature of approximately $-23\,°C$. An optical mosaic of the surface of each sample was taken using an integrated optical camera. Impurity data, including sodium, were recorded as 1D lines and 2D maps using the laser with spot size $40\,\mu m$, firing rate $300\,Hz$, and a fluence of $3.5\,J/cm^2$. After collection, uncalibrated

intensity data from the ICP-MS were corrected for background effects and drift using the software HDIP (Teledyne CETAC
90 Photon Machines), which was also used to create impurity maps.

2.4 Computational framework

The computational framework does not aim to replicate the physical processes involved in grain growth and impurity localisation but to create a statistically representative microstructure and associated impurity distribution. Its construction breaks down into the following steps.

2.4.1 LA-ICP-MS data processing

95

The grain boundary network was identified manually in the impurity maps through comparison with optical images. Pixels of high intensity in the chemical map which were located at visible grain boundaries in the optical image were considered as grain boundary pixels. High intensity pixels away from boundaries were considered to be impurities localised at dust particles, and are treated as grain-interior pixels. This approach results in a binary mask which was applied to chemical maps to separate
100 grain boundary and grain interior pixels. The intensities of these pixel classes was then recorded and turned into a probability distribution capturing the probability that a given pixel has a certain intensity.

2.4.2 Ice structure generation

A 3D Poisson Voronoi tessellation (Zheng et al., 1996) is used to create the structure of modelled ice volumes. Voronoi tessellations were produced by seeding region centres in a space, at random locations in the case of Poisson Voronoi tessellations,
105 and allowing the regions to grow until they intersect with a neighbouring region. At this intersection, a boundary between the regions is formed. The region shapes are governed by how distance is measured in the space. The generalised distance formula in three-dimensions allows calculation of the distance, D, between two points, $\mathbf{x} = (x_1, x_2, x_3)$ and $\mathbf{y} = (y_1, y_2, y_3)$

$$D(x,y) = \left(\sum_{i=1}^{3} |x_i - y_i|^p \right)^{\frac{1}{p}}. \tag{1}$$

Where $p = 2$ the resulting distance is the Euclidean distance. Changing p produces different shaped grains. This process allows
110 notional spaces with regions classified either as region (grain) interiors or region (grain) boundaries.

To match the average grain radii of a target ice sample, a suitable number of grains are seeded to create regions with the same 3D grain-number density as the physical sample, that is the same number of grains per unit volume. This process results in a space containing grains with a grain volume distribution that conforms to a gamma distribution (Ferenc and Néda, 2007), which is parameterised in the supplementary material to this paper, with a mean grain radius the same as the target ice sample.
115 To create a spatial link to the pixels of the impurity maps, the Poisson Voronoi tessellation is built in a volume comprised of voxels, the extension of pixels to three-dimensions. The modelled volume is completely populated by voxels assigned to grain

interior or boundary regions as illustrated in Fig. 2. The model treats voxels as having an edge length corresponding to the pixel edge length and, therefore, the laser spot size of the LA-ICP-MS map which it represents. This allows the dimensions of the notional volume to be tied to the dimensions of physical ice samples. Each voxel has a coordinate (x,y,z), with the X, Y, Z coordinate system illustrated in Fig. 2. The modelled space is taken to have the Z axis aligned with the down-core axis of modelled samples.

2.4.3 Impurity distribution imprint

Each voxel in the generated space is assigned a numerical value representing its impurity intensity. This value is assigned by taking the two probability distributions from empirical LA-ICP-MS mapping described in Sect. 2.4.1, one for grain boundaries and another for grain interiors, and drawing a random value from these distributions for each voxel, depending on its classification as grain or boundary. The resulting intensity distribution resembles the intensity representation shown in Fig. 2.

2.4.4 Simulating and combining signals

Simulated LA-ICP-MS signals are obtained by recording the voxel intensity at each Z position of a profile of voxels, resulting in a 1D signal at $40\,\mu m$ resolution which runs the entire Z-axis of the modelled volume. Fig. 2 illustrates the paths of two such parallel profiles as blue arrows. Intensity signals from directly adjacent profiles can be summed to create a signal simulating LA-ICP-MS data collection carried out with a larger spot size. Spatially averaged signals can be produced by taking the average of two or more adjacent or non-adjacent single-profiles signals. For spot sizes larger than $40\,\mu m$, all simulated LA-ICP-MS signals are smoothed using a 1D Gaussian kernel with a standard deviation, σ, set to the laser spot size, following the procedure described in Bohleber et al. (2021). Additional subsequent Gaussian smoothing can then be applied as a post-processing step. A CFA-like signal is simulated by summing the impurity values of all the voxels in each Z plane and applying Gaussian smoothing with a one-centimetre wide kernel. This approximates the collection of a smoothed bulk signal resulting from experimental CFA (Erhardt et al., 2023), without considering effects such as dispersion (Breton et al., 2012).

2.5 Modelled data analysis

These modelled signals were then analysed to give insight into how the underlying impurity distribution creates variability in measurement. It is assumed that centimetre-scale bulk volumes of ice have an invariant intensity distribution in the X and Y directions. This bulk-invariance also holds in the Z direction of modelled ice. This Z-invariance can be interpreted as an ice sample with an unchanging climate signal despite micro-scale variability in the spatial distribution of sodium arising from the impurity-boundary association. The bulk-invariant impurity distribution in all directions means that the mean average intensity in the space, $\bar{I}$, serves as a reference value: the intensity value that would be recorded if the entire volume were melted and measured. If some sub-volume of the modelled space is representative of the volume as a whole, it will have a mean intensity of $\bar{I}$. Therefore, if a single-profile laser signal, a spatially averaged signal resulting from the combination of several profiles, or the simulated CFA signal has an average intensity approaching $\bar{I}$ at each Z value, the signal can be considered representative
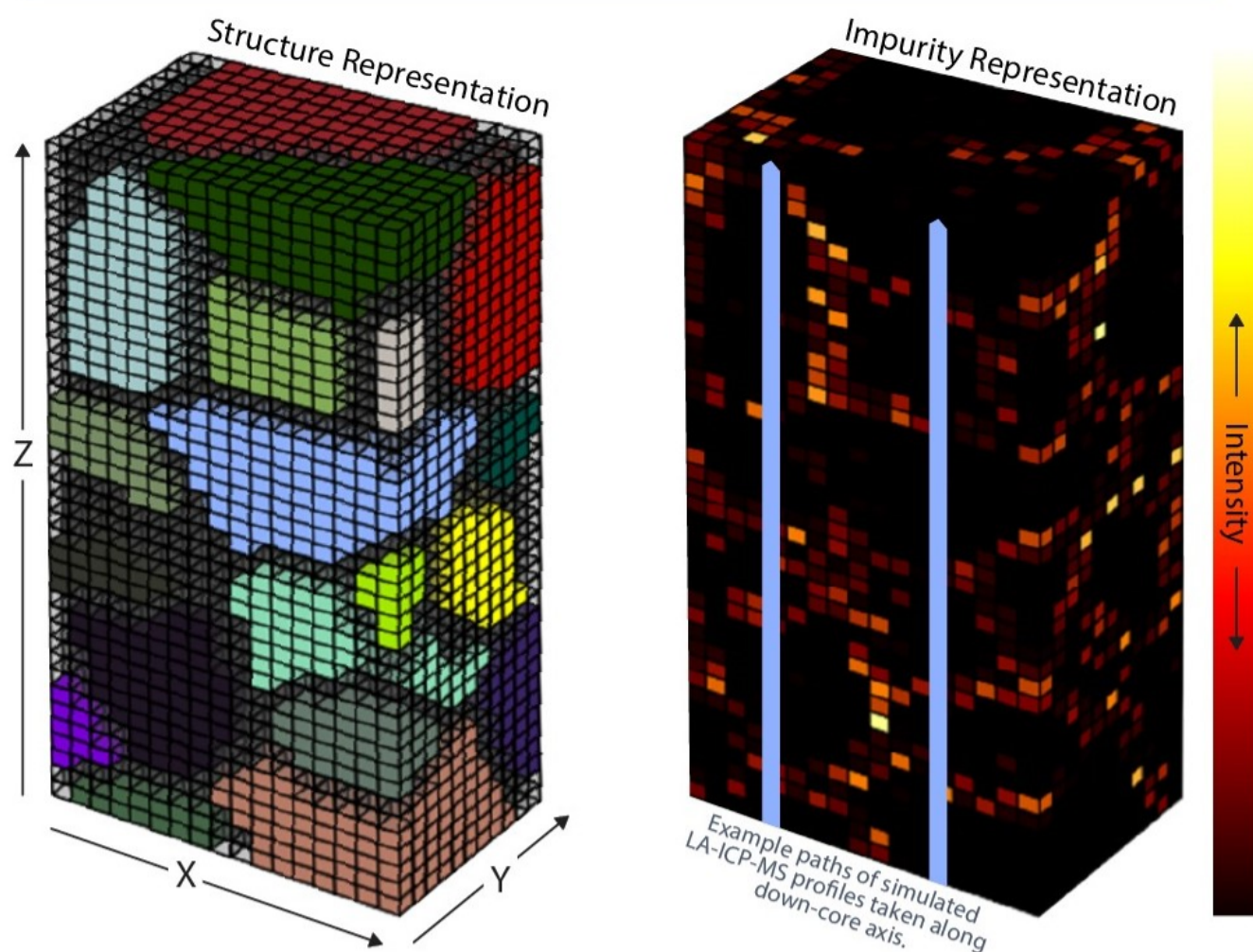
Figure 2. Visual representation of a 3D Poisson Voronoi tessellation used to represent a polycrystalline material. Each voxel, represented by a coloured cube, in the space is considered to have an edge length corresponding to the laser spot size used to measure modelled samples. The representation on the left shows the grain boundary voxels in transparent grey and each grain as a different colour. The representation on the right shows the intensity distribution imprinted on the same volume. Volumes generated for analysis are much larger than this small illustrative example, which, given a 40 μm voxel size, represents a 0.60 by 0.44 by 1.8 mm volume.

at every depth. A metric to measure how much the spatial distribution of impurities affects some signal, $I(z_i)$, or the signal representativeness, is its mean absolute deviation (MAD) from $\bar{I}$. For a signal of length l, the MAD measured in intensity units, MAD_I, is calculated as

$$MAD_I = \frac{1}{l} \sum_{i=1}^{l} |I(z_i) - \bar{I}|. \tag{2}$$

To allow easy comparison of variation between ice samples, MAD values calculated using equation 2 are reported as percentages normalised to $\bar{I}$

$$MAD = \frac{MAD_I}{\bar{I}} \times 100. \tag{3}$$

A MAD of 0 % as calculated using equation 3 represents a signal that fully captures the underlying intensity distribution at every depth interval.

3 Results

3.1 Experimental - LA-ICP-MS

All measured samples' optical and intensity maps are shown in Fig. 3, alongside the grain boundary segmentation used to isolate the grain interior and boundary intensities. A comparison of the optical images and intensity maps in Fig. 3 shows sodium is concentrated preferentially at the grain boundaries compared with grain interiors for all measured samples. This bimodal distribution is evident in Fig. 4, which shows the resulting frequency-normalised impurity distributions acquired from overlaying the boundary segmentation mask onto the intensity maps for each measured sample. All samples have higher average intensities at grain boundaries than in grain interiors. Pixels below the detection limit of the ICP-MS have their intensities recorded as zero after drift and background correction. Note that different intensity plots are not directly comparable as no calibration was performed.

Individual, spatially averaged, and smoothed signals collected from the EDC Holocene sample are shown in Fig. 5. Equivalent figures for all other measured ice samples are shown in the supplementary material. Similar to what was noted in previous studies (Bohleber et al., 2020; Della Lunga et al., 2017), experimentally collected signals vary significantly when collected at different lateral positions on the ice surface due in part to the association of impurities with grain boundaries. The two signals plotted in Fig. 5a) for the EDC Holocene sample are laterally separated by $160\,\mu m$. Even at this short distance, the signals have different numbers of peaks at varying positions and intensities. The spatially averaged signal in Fig. 5b) averages these differences somewhat, lowering overall intensity variations (note the different y-axis scale). This averaging and smoothing is further evident in Fig. 5c), a smoothed version of the data in (b).
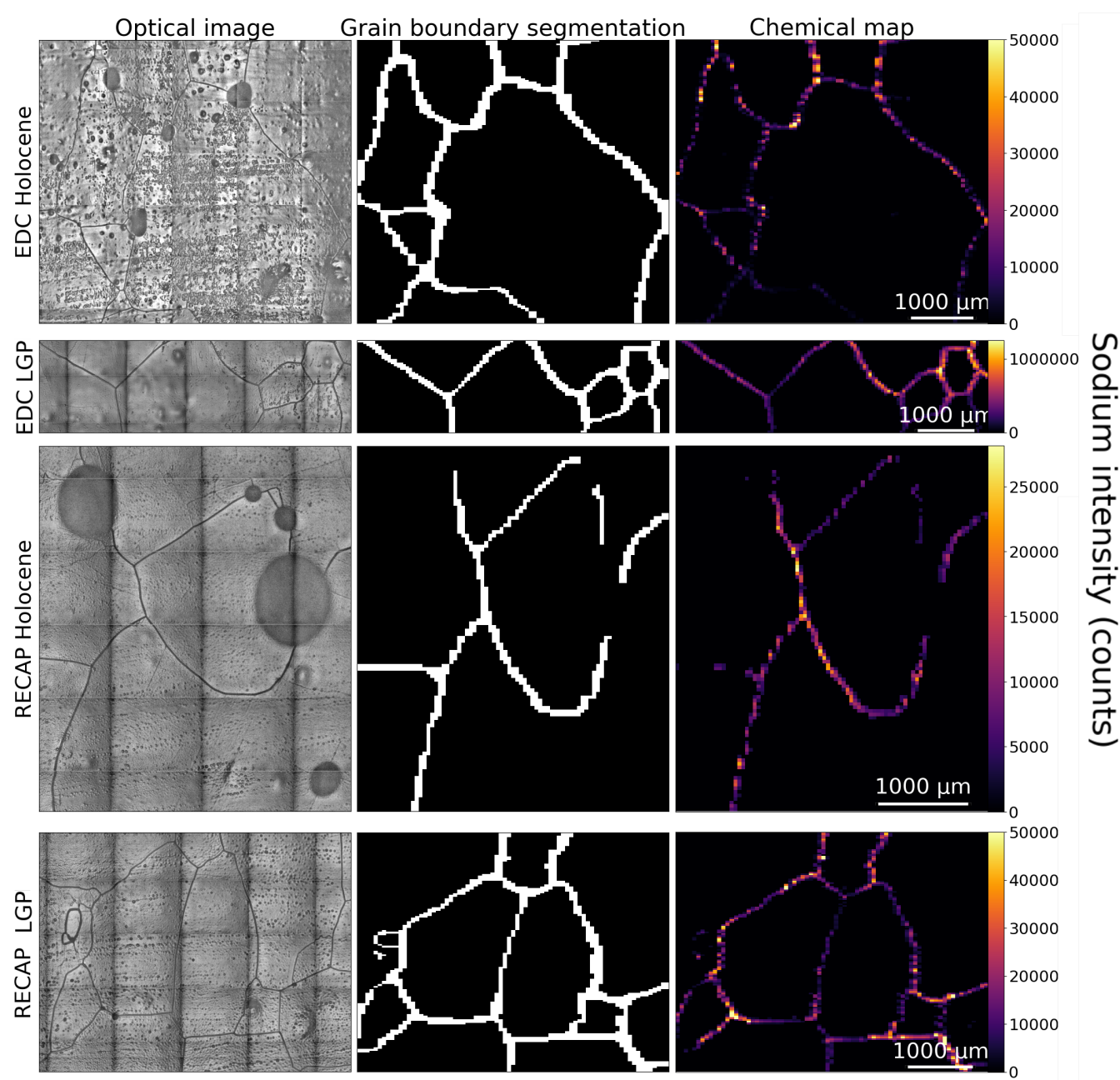
Figure 3. Columns show optical image (left), grain boundary segmentation (middle), and sodium intensity map (right) for all of the analysed samples, one sample in each row. The dark grid visible in the optical mosaics is an imaging artifact. Grain boundaries are visible as dark lines in the optical image, and bubbles as dark rounded regions. Each intensity map has its own intensity scale. The spatial scale bar relates to all images for each sample.
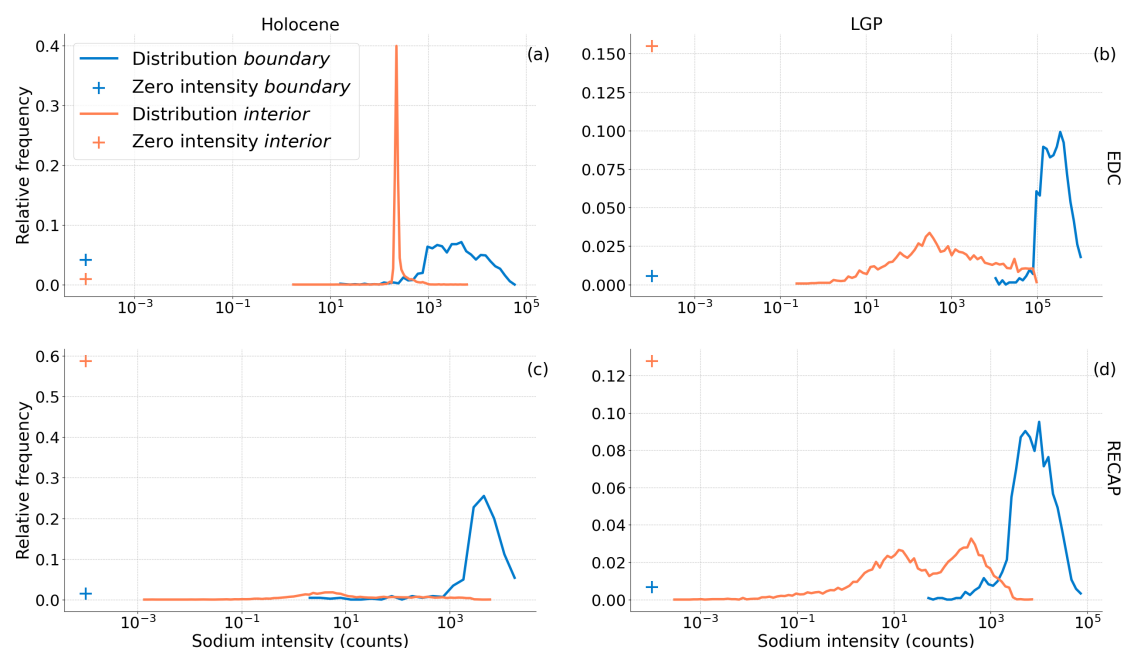
Figure 4. Sodium intensity probability distributions for all measured samples. These distributions result from the normalisation of distributions acquired from the application of binary masks which separate grain boundaries from grain interiors to the intensity maps, both shown in Fig. 3. The zero intensity cross represents pixels with intensities below the detection limit of the ICP-MS. The legend applies to all plots.

3.2 Computational

Parameterised by the grain radii reported in Table 1 and impurity distributions in Fig. 4, modelled representations of ice microstructure and impurity distribution were produced for all the analysed ice sections. All samples are modelled to have a cross-sectional area of 1 by 2 cm with lengths corresponding to the sample lengths from Table 1. This was computationally more efficient than generating a full 3.5 by 3.5 cm cross-section typically used in CFA, although no principal limitation prevents simulation of a volume of this size. The EDC and RECAP LGP samples were generated in approximately half a day using a laptop computer. The RECAP Holocene sample required more RAM to manage larger grain sizes and took 4 days to generate on a high-performance computing system. To illustrate the extremes in grain sizes, one face from each of the 3D modelled EDC Holocene and RECAP Holocene samples are shown in Fig. 6. The simulated LA-ICP-MS signals plotted for EDC Holocene in Fig. 7 originate from profiles taken along the face shown in Fig. 6 (a). Equivalent figures for all other modelled ice volumes are contained in the supplementary material.
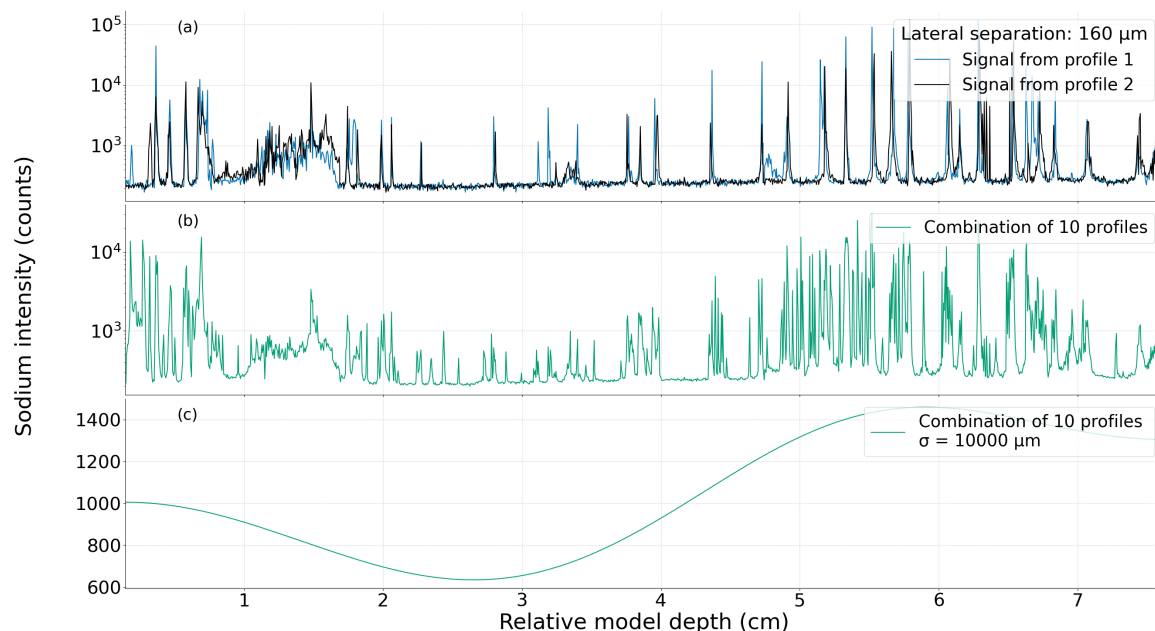
Figure 5. Measured LA-ICP-MS signals resulting from line profiles taken across the surface of the EDC Holocene sample. All profiles run down the central core axis. Panel (a) shows two signals resulting from two parallel laser tracks. Panel (b) shows the spatially averaged signal resulting from combining all measured parallel profiles, including the two signals in (a), with a range of separations between adjacent profiles. Panel (c) shows this spatially averaged signal after smoothing to CFA-resolution of 1 cm.

Fig. 7 shows signals collected under different simulated conditions, with intensity values normalised such that $\bar{I}$ has an intensity of 1. Figure 7 (a) shows two modelled signals, collected using a $40\,\mu m$ laser spot, that are separated by $160\,\mu m$, representing the modelled equivalent of the two profiles in Fig. 5 (a). These modelled signals show the same general features as experimentally measured signals, with large spikes in intensity where profiles intersect grain boundaries. Figure 7 (b) shows the result of

190 simulating two profiles, centred at the same point as those in (a), with a spot size of $120\,\mu m$, comparable to the $100\,\mu m$ spot size used in previous studies (Spaulding et al., 2017; Sneed et al., 2015), which show less variation around $\bar{I}$. The spatially averaged signal resulting from combining all $40\,\mu m$ profiles along the modelled face, shown in Fig. 6 (a), is plotted in Fig. 7 (c) and its CFA-resolution smoothed version in (d). These signals represent the largest amount of data which can be collected if limited to measuring the surface of only one face of ice samples during LA-ICP-MS, which is a common restriction for such

195 analysis. The simulated CFA signal is plotted in (e) and shows the least variation around the mean of all simulated signals.

MAD values are visualised for data collected from modelled EDC Holocene and RECAP Holocene ice in Fig. 8 with key values for all ice samples reported in Table 2. Figure 8 shows how the MAD for different signals changes based on how many
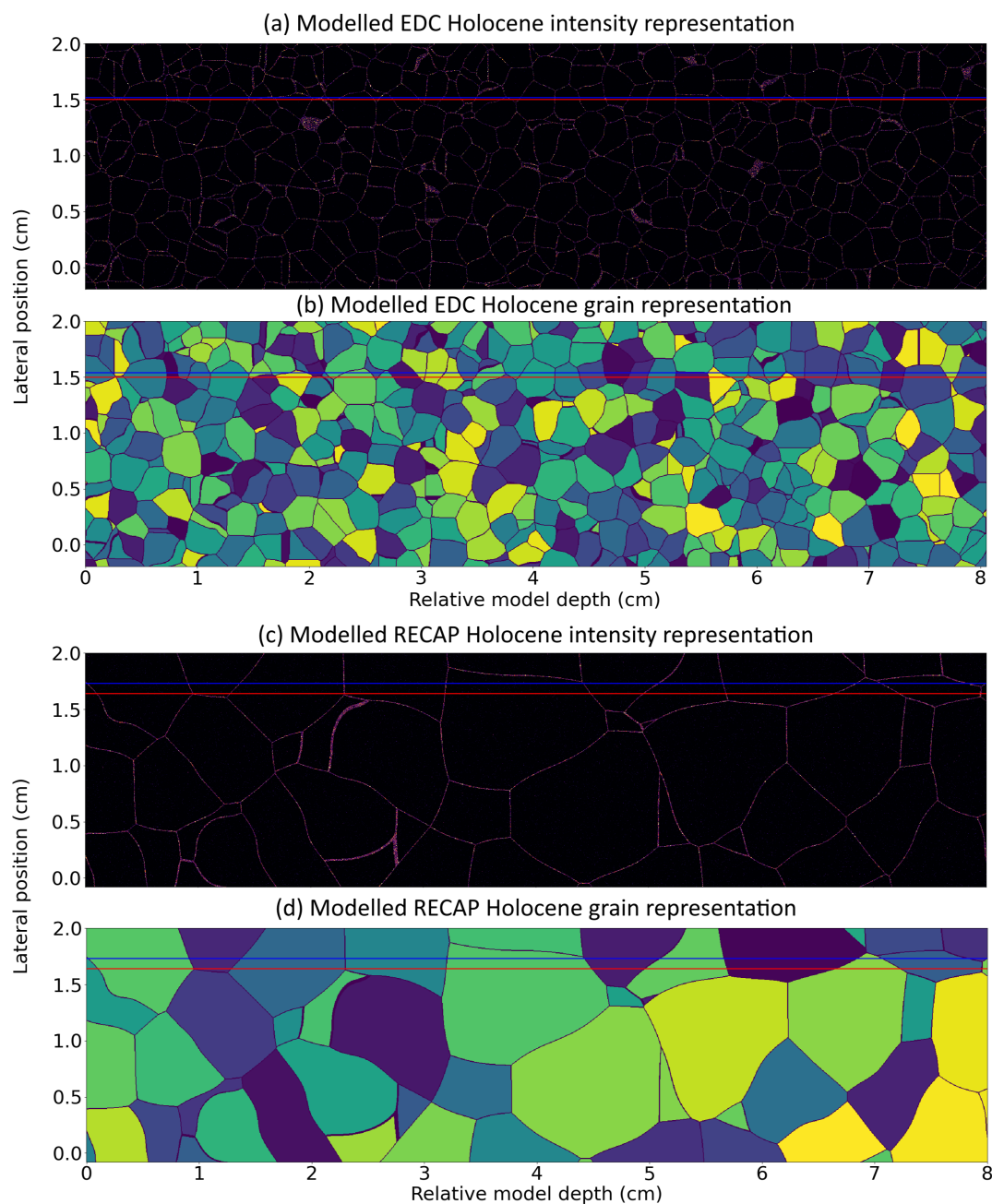
Figure 6. The intensity, (a) and (c), and structural, (b) and (d), representations of one modelled face of the EDC Holocene and RECAP Holocene samples. The structural representation shows grains as different colours, separated by grain boundaries represented in black. The colour scale for the intensity representation in (c) is the same for the experimental data shown in Fig. 3, while the colour scale in (a) has been slightly adjusted for readability. Each of the 500 rows in the intensity representation can be taken as a separate laser profile. The red and blue lines in panels (a) and (b) show the track of the profiles plotted in Fig. 7 for the EDC Holocene sample.
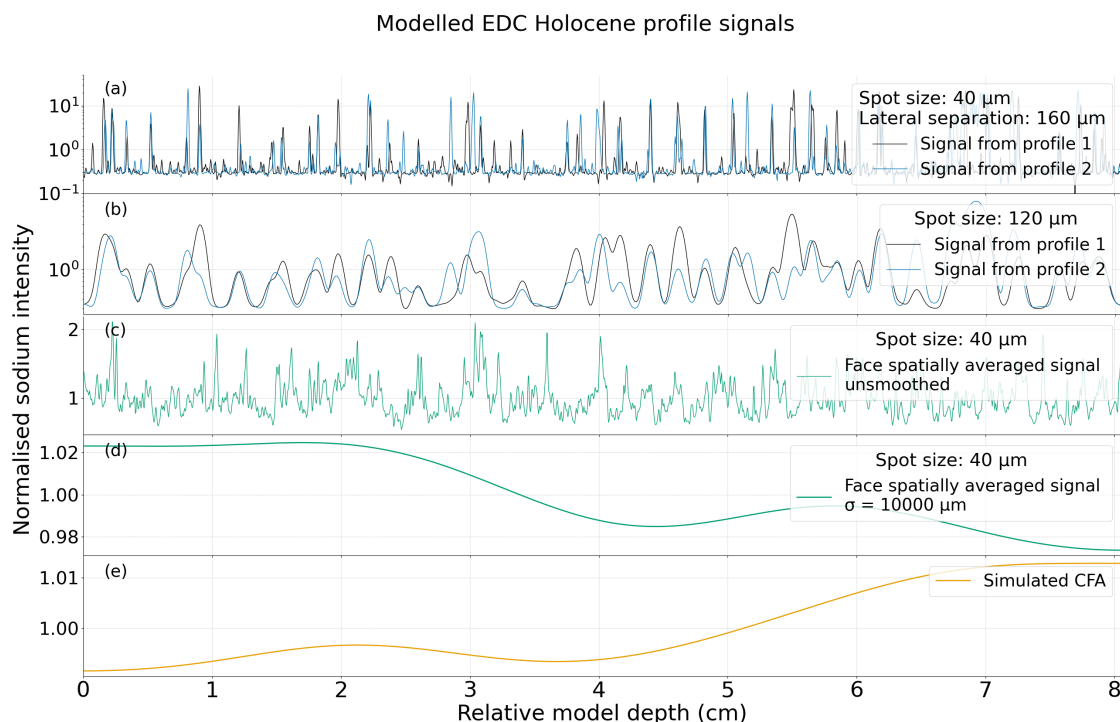
Figure 7. Line profile signals for the modelled EDC Holocene ice normalised by dividing by the volume average intensity, $\bar{I}$. Panel (a) shows signals acquired from $40\,\mu m$ spot size profiles taken from the tracks indicated in Fig. 6. Signals resulting from simulating a $120\,\mu m$ spot size along these profiles are shown in (b). The resulting signal from combining all possible profiles from the face in Fig. 6 is shown unsmoothed in (c) and smoothed to CFA resolution in (d). The simulated CFA signal is plotted in (e). Note the different y-axis scales for each panel.

profiles are combined to construct a spatially averaged signal and how much smoothing is applied. Data for the EDC Holocene sample is shown in (a) and (b) and the RECAP Holocene sample in (c) and (d). Panels (a) and (c) show data for $40\,\mu m$ spot size signals and (c) and (d) for $260\,\mu m$ spot size. The general trends are that (1) MAD decreases asymptotically as more profiles are averaged, (2) smoothing reduces signal MAD by some constant, regardless of the number of profiles a spatially averaged signal comprises, and (3) larger spot sizes produce signals with smaller MADs. These general trends hold for all measured ice intervals. For the EDC Holocene ice, single profile signals taken at $40\,\mu m$ have MADs of over 100 %, meaning that signal intensities can vary by over 100 % of the mean intensity in the space. By comparison, the simulated CFA signal, which gives the most representative signals of those simulated, has a deviation of 0.7 %. Spatially averaged signals constructed from 10 profiles, such as the signal experimentally measured and plotted in 5 (b), show variations on average of 62 % for EDC Holocene, suggesting these signals are still affected to a high degree by impurity localisation. Ice with larger grain sizes return signals (collected under the same experimental conditions) with larger MADs with the RECAP Holocene ice showing larger MAD values for all signals.

Table 2. Information on modelled sample signal representativeness. MAD values are a tabulation of key results calculated using equation 3 and are reported as the average MAD for the conditions indicated. MAD values for spatially averaged signals representing experimental conditions are calculated based on the number of profiles reported in Table 1. The best-case LA-ICP-MS MAD values apply to the specific sample geometry reported and assumes the entire width of the 2 cm face is measured.

Ice core	EDC	EDC	RECAP	RECAP
Climate period	Holocene	LGP	Holocene	LGP
MAD values (%) for experimental LA-ICP-MS conditions reported in Table 1				
Single profiles, 40 μm, unsmoothed	117	135	146	130
All profiles spatially averaged, 40 μm, unsmoothed	62	78	112	85
All profiles spatially averaged, 40 μm, $\sigma = 10\,000$ μm	6	9	15	11
CFA MAD value (%)				
Smoothed with $\sigma = 10\,000$ μm kernel	0.7	0.7	1.6	1.5
MAD values (%) for all 500 face profiles spatially averaged LA-ICP-MS				
40 μm, unsmoothed	19	26	33	24
40 μm, $\sigma = 10\,000$ μm	1.6	4.7	5.6	1.9
280 μm, unsmoothed	15	19	26	18
280 μm, $\sigma = 10\,000$ μm	1.5	4.7	5.9	1.9
Approximate increase in number of LA-ICP-MS profiles required to reduce MAD by a factor of 2				
40 μm, unsmoothed	11	13	20	13
40 μm, $\sigma = 10\,000$ μm	4	5	6	5
280 μm, unsmoothed	5	5	8	5
280 μm, $\sigma = 10\,000$ μm	4	5	5	5
Total number of spatially averaged LA-ICP-MS profiles required for less than 20 % MAD				
40 μm, unsmoothed	456	[1]-	-	-
40 μm, $\sigma = 10\,000$ μm	1	2	3	2
280 μm, unsmoothed	15	31	-	35
280 μm, $\sigma = 10\,000$ μm	1	1	2	2

[1]- indicates the value is unreachable

210   The asymptotic behavior of the MAD plots motivates calculating the number of profiles required to improve the MAD by some factor. Table 2 contains the number of profiles required to achieve a relative decrease in MAD by a factor of two. These values show that large *relative* improvement in MADs can be made by measuring a small number of extra profiles. Where an *absolute* MAD is targeted, thresholds such as the red line in each panel of Fig. 8, which illustrates reaching an arbitrary limit of 20 %, can be considered. The number of profiles required to reach this threshold is also recorded in Table 2.
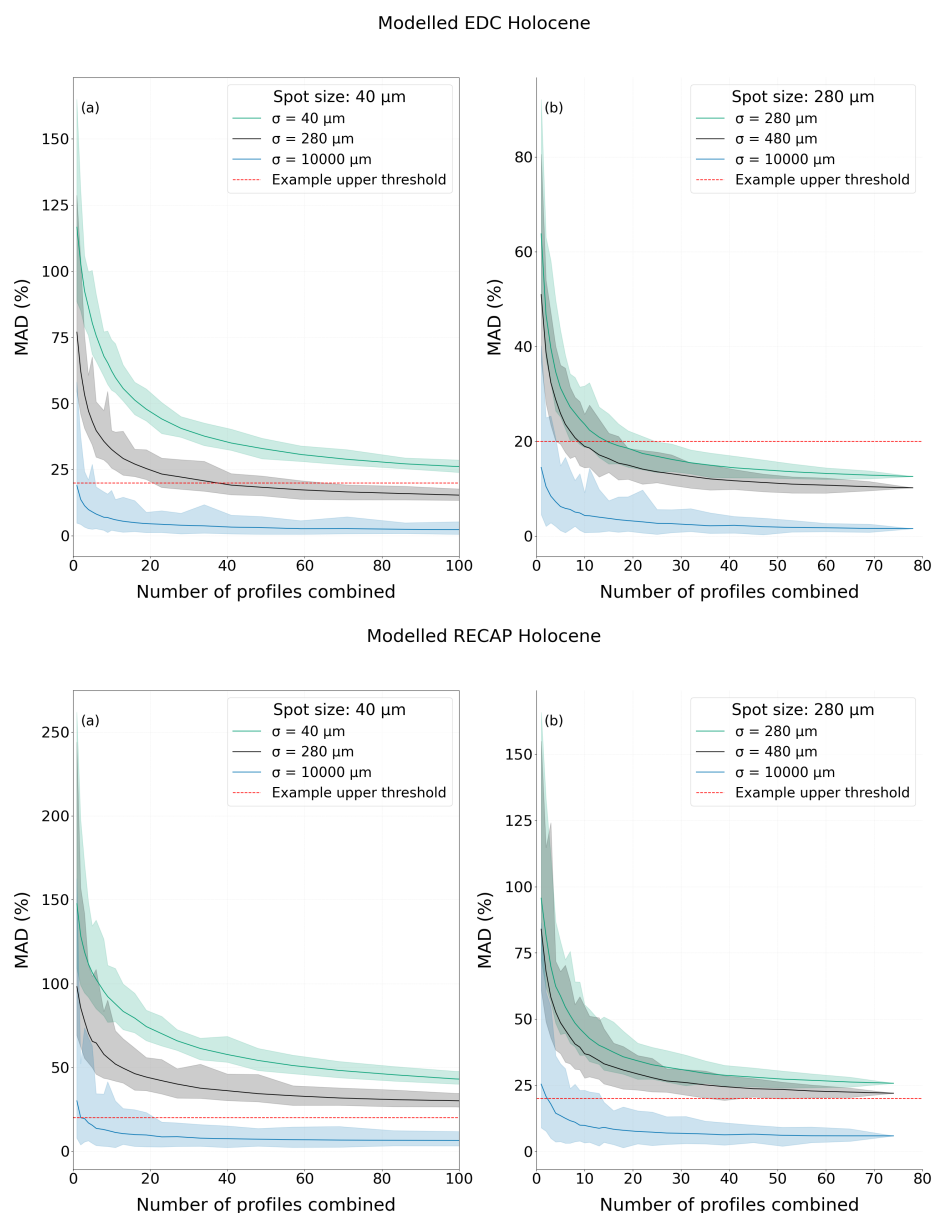
Figure 8. Plots of calculated MAD values against the number of LA-ICP-MS profiles used to construct a spatially averaged signal for the modelled EDC Holocene and RECAP Holocene faces shown in Fig. 6. As there are multiple ways to choose profiles for combination into a spatially averaged signal, the solid line of each colour shows the mean result and the shaded region shows the range of MADs acquired for different possible combined profiles. Panels (a) and (c) show results from simulating a $40\,\mu m$ laser spot and (b) and (d) a $280\,\mu m$ laser spot. Different coloured regions show MAD values resulting from smoothing with different width Gaussian kernels. An arbitrary threshold of 20 % is also shown (red line).

4 Discussion

4.1 Measured impurity distribution

The empirically measured single-line profiles in Fig. 5 (a) show large intensity spikes with clear differences between profiles separated by even short distances on the ice's surface. This is the same behaviour shown by data collected during previous LA-ICP-MS studies (e.g. Bohleber et al., 2021) and is interpreted as an effect of the localisation of impurities at grain boundaries. Combining experimentally measured profiles to make spatially averaged signals resulting in output such as that plotted in Fig. 5 (b) and subsequent smoothing, shown in (c), results in signals with less variability.

Notably, as experimentation between ice samples was carried out on different days without calibration, intensity signals are not directly comparable between plots. Here, recently developed techniques for calibrating high-resolution LA-ICP-MS data (Bohleber et al., 2024) would allow for more straightforward comparisons to be made between data taken from different core sections over different time periods.

4.2 Model suitability to represent ice samples

With comparatively small maps (a few mm^2) as input and knowledge of the local average grain size, this new framework can generate a 3D ice volume representing the ice sample's structure and impurity distribution. By design, the model's representativity of physical ice samples holds in a statistical sense, justifying the transferability of model findings back to physical ice samples. Although a one-to-one physical representation was not the target, some noteworthy analogies exist: Voronoi tessellations are frequently used to create modelled structures representing polycrystalline materials such as metals (Zheng et al., 1996). There is a phenomenological link between grains in metallic systems and glacier ice, with both material classes growing over time according to a similar growth law (Alley et al., 1986), that motivates the use of Poisson Voronoi tessellations to form the microstructure of modelled ice samples. Poisson Voronoi tessellations, glacier ice, and metals have similar grain volume distributions and grain shapes. In ice, grain shapes are typically considered isometric (Cuffey and Patterson, 2010). It was found that a distance metric with p = 3 in equation 1 produces the most appropriate shape grains for modelling ice. Changing to Euclidean distance (p=2) produces solely planar grain boundaries, and increasing p above three increases computational time with little difference in grain shapes.

With grain shapes determined by the chosen growth model, the grain volume remains the only free parameter. The mean grain volume determines the appropriate number density of seed points in the Voronoi diagram required to produce target modelled grain volumes. Therefore, estimating a representative mean grain volume or radius for the ice sample plays an important role in generating an adequate representation in the model. For the space dimensions and grain radii reported in Table 1, the modelled spaces have grains only partially contained in the modelled volume with no full grains modelled, meaning the grain volumes can not be directly estimated. This clearly adds further complexity. A detailed discussion on the grain size distribution of modelled volumes is contained in the supplementary material. This material shows that grain volumes vary around the mean grain volume conforming well to a gamma distribution. Notably, this grain volume distribution closely matches the empirically

16

observed log-normal grain volume distribution from the EDC ice core for grains at depths above 2812 m (Durand et al., 2009). Normal grain growth dominates grain evolution over recrystallisation processes at these depths at the EDC drill site. Since there is no similar study available for the RECAP ice core, we assume this grain size distribution also suitably applies to these samples. Comparing the modelled EDC Holocene face, (a) and (b) in Fig. 6, with the RECAP Holocene face, (c) and (d), illustrates how the model captures different grain sizes and impurity imprints modelled for different samples.

4.3 Framework application

LA-ICP-MS ice core analysis is seeing growing interest with several experimental setups being operated by different groups, all differing in experimental settings and spatial resolution. In this context, the framework presented here can allow improved comparison between the outputs of different experimental setups, and can form an essential foundation for inter-technique comparisons, first and foremost with CFA.

The goal of many LA-ICP-MS analyses is to collect an underlying climate signal with 1D line profiles, the interpretation of which should be invariant of the method used to collect the signal and the lateral position from which data is collected. As recognised early on, it remains doubtful whether this goal has already been achieved (Della Lunga et al., 2017) and imaging fully revealed the origin of this problem lying in the grain boundary imprint (Bohleber et al., 2020). As yet another important step forward, the modelled ice volumes produced in this work can be analysed for a variety of different ice and impurity conditions and without the constraints placed on experimental analyses. While routine experimental LA-ICP-MS currently facilitates the collection of millimetre-sized maps and 10s of profiles from the surface of ice samples, modelled volumes can be used to construct centimetre-sized maps and all possible profiles throughout a 3D volume. Furthermore, the simulation of a CFA signal allows a direct comparison of LA-ICP-MS and CFA signals which is only possible as this is a 3D model. This facilitates a direct comparison that is not currently possible for physical ice samples as the outer portion of ice measured using CFA is not measured to avoid contamination (Dallmayr et al., 2016).

The variability in experimentally acquired signals results from a superposition of different signals originating from the grain structure, ice layering, experimental settings and more. On the other hand, intentionally in its present configuration, any variation in modelled signals is due to impurity localisation, allowing this effect to be investigated in isolation. This variation is illustrated in Fig. 7, with all signals displaying some deviation from $\bar{I}$. The model allows quantification of the magnitude of this imprint across scales and makes quantitative predictions on the experimental design (e.g. how many line profiles to collect) required to managing this imprint. Notably, this application is independent of whether calibrated signals or intensities are desired.

4.3.1 Capturing a representative signal

To date, criteria guiding the collection of layer-representative signals have been suggested based on the coherence of line profiles taken (Bohleber et al., 2021) and coherence with CFA signals (Spaulding et al., 2017; Della Lunga et al., 2017). In the modelled space employed here, a signal that fully captures the underlying layer would have the value $\bar{I}$ at all positions.

Therefore signals which are coherent are likely also representative. From top to bottom, ((a) through (e)), the panels in Fig. 7
280 show convergence to $\bar{I}$. This convergence can be explained by each subsequent signal resulting from profiles that sample more
volume per unit depth or have increasing smoothing between depths. Clearly, signals that sample more material per unit depth,
such as CFA, are less influenced by variations due to the spatial distribution of impurities. Accordingly, it is not surprising that
Table 2 shows that simulated CFA signals have the lowest MADs.

Quantification of signal representativeness can be used to guide experimental design. Reported CFA MAD values are specific to
285 a hypothetical melthead with a 1 by 2 cm cross-section and would further reduce if a larger cross-sectional area (and therefore
more volume per unit depth) is melted. Comparing MADs for different samples reveals a possible motivation for requiring CFA
analysis with higher representativeness. It is evident that samples with larger grain sizes result in higher signal MADs. This
suggests that quantifying signal representativeness may become relevant for discrete and continuous bulk analysis on samples
with very large grain volumes, e.g. deep ice, as even centimetre-sized samples may only contain small numbers of grains and
290 their boundaries.

In the case of LA-ICP-MS, experimental design is also driven by resolution and representativeness requirements. The MAD
of LA-ICP-MS signals is significantly reduced when smoothed to the same resolution as CFA, therefore increasing represen-
tativeness. This vertical resolution reduction can be achieved through a combination of measuring with larger spot sizes, using
an analytical system with large vertical signal mixing, or applying smoothing in post-processing. Collecting the most repre-
295 sentative LA-ICP-MS signals requires combining and smoothing all signals on the analysed face to give a MAD of 1.5 % for
the EDC Holocene sample, approaching that of CFA. In cases where high vertical resolution is critical, signals with even lower
MAD values can be collected by analysing a larger surface area, similar to increasing the cross-sectional area of ice analysed
using CFA. This could be achieved by measuring samples with larger surface areas or by collecting profiles from a fresh, i.e.
deeper in the X or Y plane, ice surface. However, this comes at the expense of increased measurement time.

300 The requirement that many profiles must be averaged to produce high-resolution LA-ICP-MS signals with high representa-
tiveness corroborates the assertion made by Della Lunga et al. (2017), that "the averaging of the LA[-ICP-MS] signal between
two or more parallel tracks spaced by a few millimetres is not only desirable, but necessary". The asymptotic behaviour of the
MADs, shown in Fig. 8, shows that increasing the number of profiles combined into a spatially averaged signal initially returns
a large reduction in MADs, and therefore increase in signal representativeness. Table 2 shows that a *relative* increase in the
305 representativeness by a factor of 2 can be achieved by measuring an extra 11 profiles at $40\,\mu m$ spot size for the EDC Holocene
samples., and that even fewer are required to achieve the same gain with larger spot sizes and more signal smoothing.

While relative improvements are useful benchmarks, experimental design should also consider the absolute target representa-
tiveness required to capture a climate signal, the criteria for which will depend on the depth, age, and estimated layer thickness
of the target ice. To showcase a concrete example of how the model can be used to set an experimental design according to a
310 predefined limit for tolerable signal MADs, we consider an arbitrarily selected MAD of 20 % acceptable. However, this is not

a set value and should be adapted according to the objectives and analysis targets. For EDC Holocene Table 2 shows this can be achieved through collecting signals in the following ways:

- at a resolution of $40\,\mu m$ with no signal smoothing, at least 465 profiles must be collected

- at a resolution of $280\,\mu m$ with no signal smoothing, at least 9 profiles must be collected

315 - at a resolution of $280\,\mu m$ with signal smoothing to CFA resolution, at least 1 profile must be collected

These values will vary for different ice core samples, notably the collection of an unsmoothed spatially averaged profile with a MAD of less than 20 % is not possible for the modelled RECAP Holocene sample, but illustrates the need for either many profiles or low vertical resolution to achieve representativeness. Therefore through determining a target MAD and depth resolution the nature of the analysis, e.g. LA-ICP-MS or CFA, can be set to best extract a layer-representative signal at the

320 required resolution.

Under the right conditions LA-ICP-MS analysis can return signals with higher resolutions and similar representativeness to those produced using CFA. This positions LA-ICP-MS well as a tool to extract high-resolution climate signals, with the important added value of LA-ICP-MS being a micro-destructive technique, allowing revisiting of ice archives and performance of round-robin experiments among different laboratories with their own analytical strengths. Given the requirement for many

325 profiles to be measured, there is a clear benefit in increasing the spatial extent over which information is collected by LA-ICP-MS. To achieve such measurements experimental and analytical developments are required. Large sample chambers have merits (Sneed et al., 2015; Stoll et al., 2023), and this should be considered during the cutting and processing of target ice samples. However, imaging areas larger than a few mm x mm currently requires prohibitively long measurements. This restriction can be somewhat mitigated by high repetition rate LA systems which may allow chemical data to be collected over very large surface

330 areas of ice samples. The model developed here may significantly aid the design of such experiments, by a priori determining the desired spot size and resolution. This will allow representative, lateral position-invariant, signals to be collected at high-resolution using LA-ICP-MS. Yet, especially for deep ice, we will require a better understanding of how a climate signal manifests at the microscale. This involves a better understanding of the processes driving the localisation of soluble impurities at grain boundaries, possibly occurring during the transition from snow to firn and subsequently ice (Stoll et al., 2023). Related

335 effects comprise impurity diffusion (Barnes et al., 2003; Ng, 2021), for which the ice structure created by 3D Poisson Voronoi tessellations could also be a useful tool.

4.4 Potential extensions

The framework presented can be adapted to a broad range of ice samples. In particular for deep ice, implementing additional constraints will be crucial. The structure and impurity distribution of ice must be suitably captured at the grainscale, which is

340 much larger in deep ice. This entails simulation of signals over a large enough volume, which requires careful management of computational resources. The current process limiting computational performance is the speed of structure generation, which rapidly increases with increasing grain size in the current implementation. This explains the large increase in model generation

time for the RECAP Holocene sample in comparison with the other samples. To overcome this limitation a more efficient structure generation could be implemented which exploits parallel processing. Then, the following applications appear as worth-while additions to improve the model representation of various ice conditions.

The modelled ice generated in this study represents the basic structure of ice well but does not include features typical of glacier ice beyond grains and their boundaries. Ice samples contain other prominent features in their microstructure such as bubbles and insoluble impurities. Work that characterises such features can be used to amend this framework to include their effects on impurity distribution (Bohleber et al., 2023; Stoll et al., 2021; Bendel et al., 2013). Considering insoluble inclusions will allow this framework to be extended to chemical species mostly present in dust. The probability distributions describing the localisation of these elements will likely be unique for each element and therefore dimensionality reduction techniques could be useful to allow analysis to be carried out to bring insight into multiple impurities in one model.

To capture ice microstructure representative of that seen in deeper ice, grain shapes representing ice that has undergone re-crystallisation effects beyond normal grain growth will have to be generated. Ice subject to deformation undergoes dynamic recrystallisation processes that change the grain fabric (Cuffey and Patterson, 2010). The resulting structures are different to those generated by a Poisson Voronoi tessellation. A potential approach to creating such grain fabrics is to start with a microstructure such as a 3D Poisson Voronoi tessellation and model vertical ice deformation in uniaxial compression such as that seen as at ice domes. Modelling the microstructure evolution would yield a simplified combination of normal grain growth and recrystallisation processes. There is extensive literature discussing the computational modelling of microstructure recrystallisation (Hallberg, 2011). However, the redistribution of impurities under these recrystallisation processes and their impacts on the recrystallisation processes themselves must also be incorporated into such a model. Ice with more complex microstructures can also be modelled, for example, by implementing more sophisticated Voronoi tessellations to precisely capture grain volumes (Simone et al., 2017), capture grain size transitions, (Bourne et al., 2020), and implement preferred growth directions (van Nuland et al., 2021).

5 Conclusions

Extracting paleoclimate signals with single line profiles measured by LA-ICP-MS has suffered from severe ambiguities in the past. Combining many individual signals producing a spatially averaged signal has been suspected as a potential remedy, but only the framework developed here adds a quantitative dimension to this problem. To do so we employ a physical-based model of the microscopic ice chemistry constructed using empirical data collected with LA-ICP-MS and a 3D model of the ice matrix represented by a Poisson Voronoi structure. The framework is designed to quantitatively assess the imprint of the ice matrix, the grain boundary network, in 1D signals collected with LA-ICP-MS for various ice conditions. These conditions are captured in samples analysed from both Greenland and Antarctica from both the Holocene and Last Glacial Period. Results show that a spatially averaged signal resulting from the combination of all profiles on a modelled ice sample's face varies on average by between 19 to 33 % in the presented cases, with increasing deviation for samples with larger average grain sizes. This variation

375   can be further reduced to between 1.5 and 5.9 % by smoothing these signals with a Gaussian kernel to CFA resolution. Further additions to this framework are foreseen to extend the representation also to insoluble impurities and a broader range of ice conditions. This framework provides a much needed tool for quantitative guidance in setting experimental parameters in LA-ICP-MS, which are important for both, ice-impurity interactions and the layering commonly associated with climactic signals. Considering the evident merits of LA-ICP-MS delivering high-resolution impurity signals in a micro-destructive fashion, this

380   approach may become particularly crucial for the systematic planning of the collection of data from deep ice samples. This especially concerns ice collected from the ongoing efforts to retrieve the oldest continuous ice record from Antarctica and its interpretation.

Code and data availability. Datasets and code will be made publicly available via open-access repositories such as those facilitated by GitHub, Pangaea (www.pangaea.de) or Zenodo (www.zenodo.org) after acceptance of the manuscript.

385 *Author contributions.* Experimental measurements were designed and conducted by PL, PB, and NS. Software was written by PL with conceptualisation and support provided by PB and RR. The scope of the manuscript was developed by PL, RR, and PB and an initial manuscript draft was produced by PL. All authors contributed to the discussion of the results and the final version of the manuscript.

Competing interests. The authors declare that they have no conflict of interest.

References

Abram, N., Wolff, E., and Curran, M.: A review of sea ice proxy information from polar ice cores, Quat. Sci. Rev., 79, 168–183, https://doi.org/https://doi.org/10.1016/j.quascirev.2013.01.011, 2013.

Alley, R., Perepezko, J., and Bentley, C.: Grain Growth in Polar Ice: I. Theory, Journal of Glaciology, 32, 415–424, https://doi.org/https://doi.org/10.3189/S0022143000012120, 1986.

Barnes, P., Wolff, E., Mader, H., Udisti, R., Castellano, E., and Röthlisberger, R.: Evolution of chemical peak shapes in the Dome C, Antarctica, ice core, J. Geophys. Res., 108, https://doi.org/https://doi.org/10.1029/2002JD002538, 2003.

Bendel, V., Ueltzhöffer, K., Freitag, J., Kipfstuhl, S., Kuhs, W., Garbe, C., and Faria, S.: High-resolution variations in size, number and arrangement of air bubbles in the EPICA DML (Antarctica) ice core, Journal of Glaciology, 59, 972–980, https://doi.org/https://doi.org/10.3189/2013JoG12J245, 2013.

Bohleber, P., Roman, M., Šala, M., and Barbante, C.: Imaging the impurity distribution in glacier ice cores with LA-ICP-MS, J. Anal. At. Spectrom., 35, 2204–2212, https://doi.org/http://dx.doi.org/10.1039/D0JA00170H, 2020.

Bohleber, P., Roman, M., Šala, M., Delmonte, B., Stenni, B., and Barbante, C.: Two-dimensional impurity imaging in deep Antarctic ice cores: snapshots of three climatic periods and implications for high-resolution signal interpretation, The Cryosphere, 15, 3523–3538, https://doi.org/https://doi.org/10.5194/tc-15-3523-2021, 2021.

Bohleber, P., Stoll, N., Rittner, M., Roman, M., Weikusat, I., and Barbante, C.: Geochemical Characterization of Insoluble Particle Clusters in Ice Cores Using Two-Dimensional Impurity Imaging, Geochemistry, Geophysics, Geosystems, 24, https://doi.org/https://doi.org/10.1029/2022gc010595, 2023.

Bohleber, P., Larkman, P., Stoll, N., Clases, D., Gonzalez de Vega, R., Šala, M., Roman, M., and Barbante, C.: Quantitative insights on impurities in ice cores at the micro-scale from calibrated LA-ICP-MS imaging, Geochem. Geophys. Geosyst., 25, https://doi.org/https://doi.org/10.1029/2023GC011425, 2024.

Bouchet, M., Landais, A., Grisart, A., Parrenin, F., Prié, F., Jacob, R., Fourré, E., Capron, E., Raynaud, D., Lipenkov, V., Loutre, M.-F., Extier, T., Svensson, A., Legrain, E., Martinerie, P., Leuenberger, M., Jiang, W., Ritterbusch, F., Lu, Z.-T., and Yang, G.-M.: The Antarctic Ice Core Chronology 2023 (AICC2023) chronological framework and associated timescale for the European Project for Ice Coring in Antarctica (EPICA) Dome C ice core, Clim. Past, 19, 2257–2286, https://doi.org/https://doi.org/10.5194/cp-19-2257-2023, 2023.

Bourne, D., Kok, P., Roper, S. M., and Spanjer, W.: Laguerre tessellations and polycrystalline microstructures: a fast algorithm for generating grains of given volumes, Philosophical Magazine, 100, 2677–2707, https://doi.org/https://doi.org/10.1080/14786435.2020.1790053, 2020.

Breton, D., Koffman, B., Kurbatov, A., Kreutz, K., and Hamilton, G.: Quantifying Signal Dispersion in a Hybrid Ice Core Melting System, Environmental Science & Technology, 46, 11 922–11 928, https://doi.org/https://doi.org/10.1021/es302041k, 2012.

Brook, E. and Buizert, C.: Antarctic and global climate history viewed from ice cores, Nature, 558, 200–208, https://doi.org/https://doi.org/10.1038/s41586-018-0172-5, 2018.

Chung, A., Parrenin, F., Steinhage, D., Mulvaney, R., Martín, C., Cavitte, M., Lilien, D., Helm, V., Taylor, D., Gogineni, P., Ritz, C., Frezzotti, M., O'Neill, C., Miller, H., Dahl-Jensen, D., and Eisen, O.: Stagnant ice and age modelling in the Dome C region, Antarctica, The Cryosphere, 17, 3461–3483, https://doi.org/https://doi.org/10.5194/tc-17-3461-2023, 2023.

Cuffey, K. and Patterson, W.: The Physics of Glaciers, Elsevier, 4 edn., 2010.

Dallmayr, R., Goto-Azuma, K., Astrid KjÆr, H., Azuma, N., Takata, M., Schüpbach, S., and Hirabayashi, M.: A high-resolution continuous flow analysis system for polar ice cores, Bull. Glaciol. Res., 34, 11–20, https://doi.org/https://doi.org/10.5331/bgr.16R03, 2016.

Della Lunga, D., Müller, W., Rasmussen, S. O., Svensson, A., and Vallelonga, P.: Calibrated cryo-cell UV-LA-ICPMS elemental concentra-
440   tions from the NGRIP ice core reveal abrupt, sub-annual variability in dust across the GI-21.2 interstadial period, The Cryosphere, 11,
       1297–1309, https://doi.org/https://doi.org/10.5194/tc-11-1297-2017, 2017.

Durand, G., Svensson, A., Persson, A., Gagliardini, O., Gillet-Chaulet, F., Sjolte, J., Montagnat, M., and Dahl-Jensen, D.: Evolution of the
       texture along the EPICA Dome C ice core, LowTemp. Sci., p. 91–105, https://doi.org/DOI not available, 2009.

EPICA community members, .: Eight glacial cycles from an Antarctic ice core, Nature, 429, 623–628,
445   https://doi.org/https://doi.org/10.1038/nature02599, 2004.

Erhardt, T., Jensen, C., Adolphi, F., Kjær, H., Dallmayr, R., Twarloh, B., Behrens, M., Hirabayashi, M., Fukuda, K., Ogata, J., Burgay, F.,
       Scoto, F., Crotti, I., Spagnesi, A., Maffezzoli, N., Segato, D., Paleari, C., Mekhaldi, F., Muscheler, R., Darfeuil, S., and Fischer, H.: High-
       resolution aerosol data from the top 3.8 kyr of the East Greenland Ice coring Project (EGRIP) ice core, Earth System Science Data, 15,
       5079–5091, https://doi.org/https://doi.org/10.5194/essd-15-5079-2023, 2023.

450   Ferenc, J.-S. and Néda, S.: On the size distribution of Poisson Voronoi cells, Physica A: Statistical Mechanics and its Applications, 385,
       518–526, https://doi.org/https://doi.org/10.1016/j.physa.2007.07.063, 2007.

Hallberg, H.: Approaches to modeling of recrystallization, Metals, 1, 16–48, https://doi.org/https://doi.org/10.3390/met1010016, 2011.

Kaufmann, P., Federer, U., Hutterli, M., Bigler, M., Schüpbach, S., Ruth, U., Schmitt, J., and Stocker, T.: An improved con-
       tinuous flow analysis system for high-resolution field measurements on ice cores, Environ. Sci. Technol., 42, 8044–8050,
455   https://doi.org/https://doi.org/10.1021/es8007722, 2008.

Legrand, M. and Mayewski, P.: Glaciochemistry of polar ice cores: A review, Reviews of Geophysics, 35, 219–243,
       https://doi.org/https://doi.org/10.1029/96RG03527, 1997.

Loulergue, L., Schilt, A., Spahni, R., Masson-Delmotte, V., Blunier, T., Lemieux, B., Barnola, J.-M., Raynaud, D., S, T. F., and
       Chappellaz, J.: Orbital and millennial-scale features of atmospheric CH4 over the past 800,000 years, Nature, 453, 383–386,
460   https://doi.org/https://doi.org/10.1038/nature06950, 2008.

Müller, W., Shelley, J., and Rasmussen, S.: Direct chemical analysis of frozen ice cores by UV-laser ablation ICPMS, J. Anal. At. Spectrom.,
       26, 2391–2395, https://doi.org/https://doi.org/10.1039/C1JA10242G, 2011.

Ng, F.: Pervasive diffusion of climate signals recorded in ice-vein ionic impurities, The Cryosphere, 15, 1787–1810,
       https://doi.org/https://doi.org/10.5194/tc-15-1787-2021, 2021.

465   Reinhardt, H., Kriews, M., Miller, H., Schrems, O., Lüdke, C., Hoffmann, E., and Skole, J.: Laser ablation inductively coupled plasma mass
       spectrometry: a new tool for trace element analysis in ice cores, Fresenius J. Anal. Chem., 370, 629–636, 2001.

Simone, F., Jiawei, J., De Cola, F., and Petrinic, N.: Generation of 3D polycrystalline microstructures with a conditioned Laguerre-Voronoi
       tessellation technique, Computational Materials Science, 136, 20–28, https://doi.org/https://doi.org/10.1016/j.commatsci.2017.04.018,
       2017.

470   Simonsen, M., Baccolo, G., Blunier, T., Borunda, A., Delmonte, B., Frei, R., Goldstein, S., Grinsted, A., Kjær, H., Sowers, T., Svensson,
       A., Vinther, B., Vladimirova, D., Winckler, G., Winstrup, M., and Vallelonga, P.: East Greenland ice core dust record reveals timing of
       Greenland ice sheet advance and retreat, Nature Communications, 10, 4494, https://doi.org/https://doi.org/10.1038/s41467-019-12546-2,
       2019.

Sneed, S., Mayewski, P., Sayre, W., Handley, M., Kurbatov, A., Taylor, K., Bohleber, P., Wagenbach, D., Erhardt, T., and Spauld-
475   ing, N.: New LA-ICP-MS cryocell and calibration technique for sub-millimeter analysis of ice cores, J. Glaciol., 61, 233–242,
       https://doi.org/10.3189/2015JoG14J139, 2015.

Spaulding, N., Sneed, S., Handley, M., Bohleber, P., Kurbatov, A., Pearce, N., Erhardt, T., and Mayewski, P.: A new multielement method for LA-ICP-MS data acquisition from glacier ice cores, Environ. Sci. Technol., 51, 13 282–13 287, https://doi.org/https://doi.org/10.1021/acs.est.7b03950, 2017.

480   Stauffer, B., Flückiger, J., Wolff, E., and Barnes, P.: The EPICA deep ice cores: first results and perspectives, Annals of Glaciology, 39, 93–100, https://doi.org/https://doi.org/10.3189/172756404781814500, 2004.

Stoll, N., Eichler, J., Hörhold, M., Shigeyama, W., and Weikusat, I.: A review of the microstructural location of impurities in polar ice and their impacts on deformation, Frontiers in Earth Science, 8, https://doi.org/https://doi.org/10.3389/feart.2020.615613, 2021.

Stoll, N., Bohleber, P., Dallmayr, R., Wilhelms, F., Barbante, C., and Weikusat, I.: The new frontier of microstructural impurity research in
485   polar ice, Annals of Glaciology, 64, 63–66, https://doi.org/https://doi.org/10.1017/aog.2023.61, 2023.

van Nuland, T., van Dommelen, J., and Geers, M.: An anisotropic Voronoi algorithm for generating poly-crystalline microstructures with preferred growth directions, Computational Materials Science, 186, 109 947, https://doi.org/https://doi.org/10.1016/j.commatsci.2020.109947, 2021.

Weikusat, I., Gebhardt, L., Jansen, D., Stoll, N., and Kipfstuhl, S.: Crystal c-axes (fabric analyser G50) of ice core samples (vertical thin
490   sections) collected from the polar ice core RECAP, 115-534 m depth, 2024.

Zheng, X., Sun, T., Zhou, J., Zhang, R., and Ming, P.: Modeling of Polycrystalline Material Microstructure with 3D Grain Boundary Based on Laguerre and Voronoi Tessellation, Materials, 15, https://doi.org/https://doi.org/10.3390/ma15061996, 1996.